

Realization of a crosstalk-free multi-ion node for long-distance quantum networking

P.-C. Lai,^{1,*} Y. Wang,^{1,*} J.-X. Shi,^{1,*} Z.-B. Cui,¹ Z.-Q. Wang,¹ S. Zhang,¹ P.-Y. Liu,¹ Z.-C. Tian,¹ Y.-D. Sun,¹ X.-Y. Chang,¹ B.-X. Qi,¹ Y.-Y. Huang,¹ Z.-C. Zhou,^{1,2} Y.-K. Wu,^{1,2} Y. Xu,^{1,2} Y.-F. Pu,^{1,2,†} and L.-M. Duan^{1,2,‡}

¹Center for Quantum Information, Institute for Interdisciplinary Information Sciences, Tsinghua University, Beijing 100084, PR China

²Hefei National Laboratory, Hefei 230088, PR China

Trapped atomic ions constitute one of the leading physical platforms for building the quantum repeater nodes to realize large-scale quantum networks. In a long-distance trapped-ion quantum network, it is essential to have crosstalk-free dual-type qubits: one type, called the communication qubit, to establish entangling interface with telecom photons; and the other type, called the memory qubit, to store quantum information immune from photon scattering under entangling attempts. Here, we report the first experimental implementation of a telecom-compatible and crosstalk-free quantum network node based on two trapped $^{40}\text{Ca}^+$ ions. The memory qubit is encoded on a long-lived metastable level to avoid crosstalk with the communication qubit encoded in another subspace of the same ion species, and a quantum wavelength conversion module is employed to generate ion-photon entanglement over a 12 km fiber in a heralded style. Our work therefore constitutes an important step towards the realization of quantum repeaters and long-distance quantum networks.

A future large-scale quantum network can link different functional nodes together via photonic channels [1–7], and enable numerous applications such as distributed quantum computing [8], networked quantum sensing [9–11], and global quantum communication [4, 5, 12, 13] with unprecedented performances. Recent advances on quantum networks have been achieved on various physical systems [11–22]. Among all these different physical platforms, trapped atomic ions constitute one of the most promising systems to build quantum repeater nodes for scalable quantum networks, as the highest fidelities in quantum logic operations and state detection [23, 24] have been demonstrated on this platform, which are important for the entanglement swapping [25–27], distillation [18, 19], and error correction [24] operations required in a large-scale quantum network. Other advantages include the long coherence time at the scale of a hour [28], and the record-high fidelity and rate in entangling two network nodes [14, 15].

To enable a long-distance trapped-ion quantum network, crosstalk-free dual-type qubits on each node and the interface of the node with the telecom photons are two essential requirements [29–31]. For dual-type qubits on each node, it is required that the memory qubits are employed to store quantum information for later computational tasks or establishment of remote entanglement, while the communication qubits are interfaced with photons to link different network nodes or used occasionally for sympathetic cooling. The memory qubits and the communication qubits are required to be spectrally separated so that the scattered photons during cooling, pumping, detection, and entangling attempts on the communication qubit have no detrimental influence on the state stored in the memory qubits. The memory and the communication qubits can be implemented either by employing two different ion isotopes [15, 16], or by the same ion species but exploiting a dual-type encoding with two sets of spectrally separated qubit

states [32–34]. Another requisite for a long-distance quantum network is that the network node should be interfaced with photons in the telecom band to minimize the transmission loss in optical fibers. This requirement has been fulfilled either by employing atomic transitions at the telecom band [35–38], or by converting the emitted photon to the telecom wavelength on an additional module [13, 21, 25, 39, 40]. Implementation of the above two essential requirements for a long-distance quantum network together in a single node is experimentally very challenging and has not been achieved so far in a trapped-ion system.

In this work, we report the first experimental realization of a crosstalk-free and telecom-compatible quantum network node based on two $^{40}\text{Ca}^+$ ions in a dual-type style. The memory qubit is encoded on a metastable level which is unaffected by the photon-scattering operations on the communication qubit due to the large frequency difference. The two types of qubits can be coherently converted back and forth by a Raman and a quadrupole transition. A quantum frequency conversion module is employed to convert the near-infrared photon emitted from the ion to the telecom band, and the heralded ion-photon entanglement has been demonstrated over different fiber lengths at 3 m, 1 km, and 12 km. We characterize the performance of the memory qubit with the measured coherence time about 323(19) ms and confirm that quantum information is protected in the memory qubit under repeated entangling attempts on the neighboring communication qubits until a successful record of remote ion-photon entanglement over the 12 km fiber. With all these achievements, we implement a promising quantum node based on trapped ions which fulfils the essential requirements for a long-distance quantum network.

The quantum network node is based on two $^{40}\text{Ca}^+$ ions in a segmented blade trap, with trapping frequencies at $(\omega_x, \omega_y, \omega_z) = 2\pi \times (1.65, 1.55, 0.5)$ MHz in three dimensions and the separation between two ions at $9 \mu\text{m}$. The magnetic field is along the axial direction of the trap and set to 4.2 G in the experiment (see Fig. 1A). Here the communication qubit stays in a closed 3-level subspace containing $|S_{1/2}\rangle$, $|D_{3/2}\rangle$, and $|P_{1/2}\rangle$ (see Fig. 1B), so that all the dissipative

*These authors contributed equally to this work

†Electronic address: puyf@tsinghua.edu.cn

‡Electronic address: lmduan@tsinghua.edu.cn

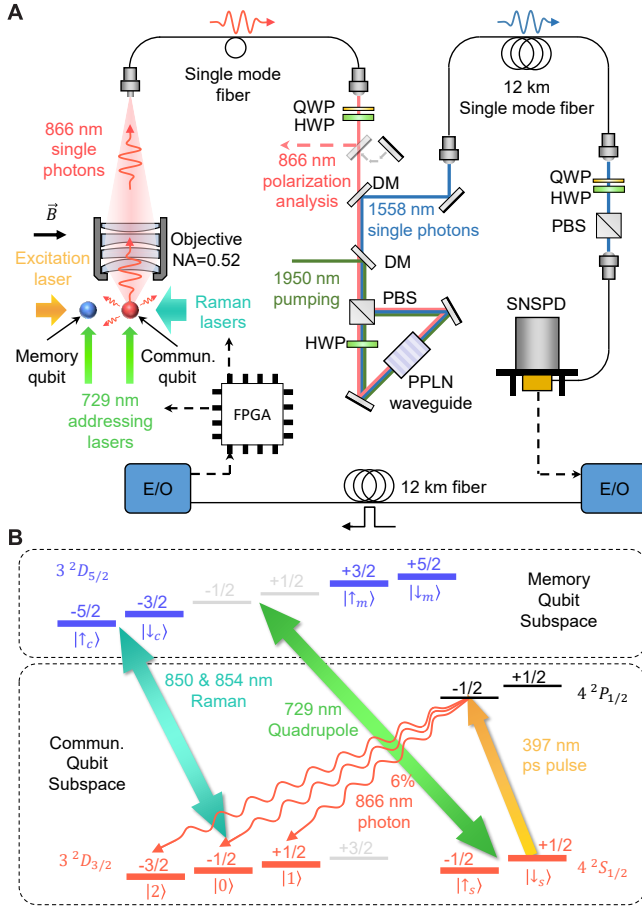


FIG. 1: Experimental setup and crosstalk-free qubit subspaces. (A) The two-ion quantum network node consists of a communication qubit and a memory qubit encoded in different subspaces of $^{40}\text{Ca}^+$ ion. The emitted single photons from the communication qubit at 866 nm are collected with a high-NA objective and are further converted to 1558 nm for transmission in a long fiber. The 729 nm beam is individually addressed. All other beams are global. (B) Two spectrally-separated subspaces for the communication qubit and the memory qubit. The communication qubit subspace is a closed three-level cycle, and the memory qubit subspace is a metastable level which is isolated from all the dissipative operations on the communication qubit, thus is suitable for storing quantum information. Bridges connecting these two subspaces include 850 nm/854 nm Raman and 729 nm quadrupole transitions. Ion-photon entanglement is excited by a 397 nm picosecond pulse.

operations on the communication qubit including cooling, optical pumping, fluorescence detection and photon excitation can be carried out by lasers at 397 nm and 866 nm in this subspace, and the fluorescent photons scattered from the communication qubit are also at these two wavelengths (or at 732 nm with a very rare chance, see Fig. S1 for the full energy levels and transitions). On the other hand, the metastable level $|D_{5/2}\rangle$ can only be driven by two transitions at 854 nm or 729 nm, which are perfectly isolated in frequency from the lasers or scattered photons for the operations on the communication qubit. In addition, the communication qubit subspace is

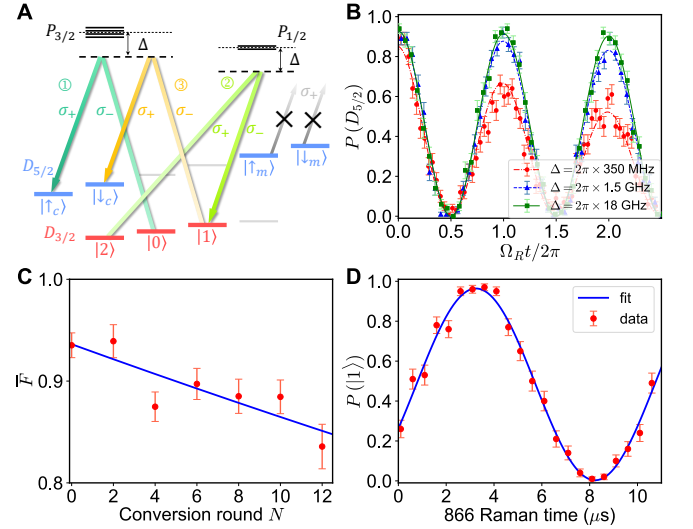


FIG. 2: Connecting communication and memory qubit subspaces through Raman transitions. (A) After a photon is detected, we use three successive Raman transitions to combine two energy levels related to $|\sigma^\pm\rangle$ photon emission and map the ion state from the communication qubit subspace to memory qubit subspace for further state manipulation and detection. (B) We measure the probability of unwanted excitation to the upper state during the Raman process with variable detunings at 350 MHz, 1.5 GHz and 18 GHz. We prepare the ion to $|\uparrow_c\rangle$ and perform a Raman pulse driving the transition $|\uparrow_c\rangle \leftrightarrow |0\rangle$ for different time and detuning. The chance of off-resonant excitation to the upper state is 12(1)%, 2.7(3)% and 0.7(2)% for detunings at 350 MHz, 1.5 GHz and 18 GHz every π -pulse. (C) We measure the state transfer fidelity between the memory qubit subspace bases $|\uparrow_c\rangle/|\downarrow_c\rangle$ and the communication qubit subspace bases $|0\rangle/|1\rangle$, with different rounds of π pulses. The fitted π -pulse fidelity is 99.2(2)% averaged on six mutually unbiased states. (D) Rabi oscillation driven by a 866 nm/866 nm Raman transition. The initial $\frac{1}{2}|\uparrow\rangle + \frac{\sqrt{3}}{2}|\downarrow\rangle$ state can be combined to $|1\rangle$ with a fidelity of 96(2)% by a $\frac{2}{3}\pi$ -pulse.

closed under the driving with 397 nm and 866 nm laser beams, so there is no need of inter-subspace repumping during the operations. Therefore we use $|D_{5/2}\rangle$ subspace to carry the memory qubit, which can store quantum information without being influenced by the operations on the communication qubit.

There are two methods to connect these two qubit subspaces, as shown in Fig. 1B. The first is the standard quadrupole transition at 729 nm which connects the $|S_{1/2}\rangle$ level in the communication qubit subspace and $|D_{5/2}\rangle$ level in the memory qubit subspace. The 729 nm beam is focused on each ion with a Gaussian radius of $2\ \mu\text{m}$ via an addressing system based on two crossed acoustic optical deflectors (AODs) and an objective with NA (numerical aperture) = 0.24. The typical fidelity of a 729 nm π -pulse is about 99% in this experiment.

The second bridge is a Raman transition by two lasers at 850 nm and 854 nm, which connects $|D_{3/2}\rangle$ level and $|D_{5/2}\rangle$ level in different subspaces, as shown in Fig. 2A. The two beams co-propagate along the magnetic field axis in complementary circular polarizations, which drive Raman

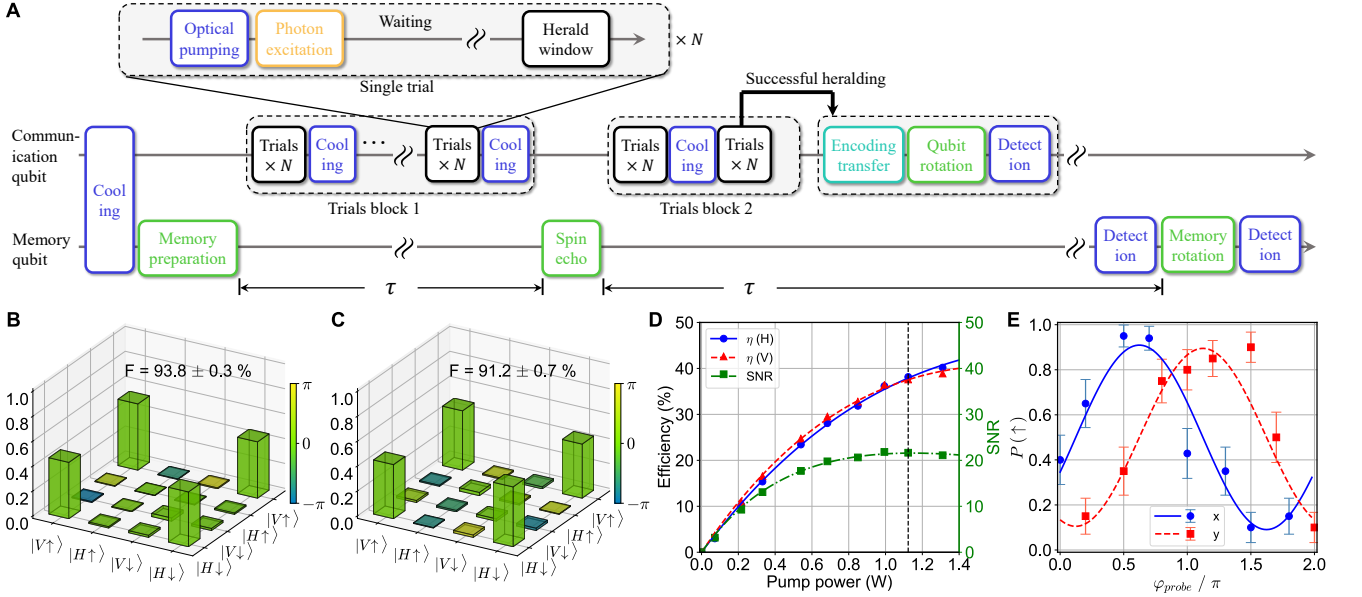


FIG. 3: The experimental protocol and heralded ion-photon entanglement at different fiber lengths. (A) The protocol used in this experiment. (B-C) Reconstructed density matrix for the ion-photon entangled state with fiber lengths of 3 m/1 km and $2\tau = 40$ ms/200 ms. The entanglement fidelity is 93.8(3)% and 91.2(7)% in each case. (D) The performance of frequency conversion. We use laser power at about 1.1 Watt (dashed line) for each polarization. (E) Measure the coherence of the ion-photon entangled state over 12 km fiber by projecting photons at $|H\rangle + |V\rangle$ (blue circle) or $|H\rangle + i|V\rangle$ bases (red square) and measuring the visibility of sinusoidal oscillations with different phases of 729 nm rotations.

transitions between $|D_{3/2}, m\rangle$ and $|D_{5/2}, m-2\rangle$ ($m = -1/2, +1/2, +3/2$). Here we set the Raman detuning Δ to 18 GHz with the chance of unwanted excitation to the intermediate state $|P_{3/2}\rangle$ at about 0.7(2)% per π -pulse, as illustrated in Fig. 2B. We demonstrate the coherent state transfer between a memory qubit subspace encoding on $|\uparrow_c\rangle/|\downarrow_c\rangle \equiv |D_{5/2}, m = -5/2\rangle/|D_{5/2}, m = -3/2\rangle$ and a communication qubit subspace encoding on $|0\rangle/|1\rangle \equiv |D_{3/2}, m = -1/2\rangle/|D_{3/2}, m = +1/2\rangle$, by two successive Raman π -pulses which drive the transitions $|\uparrow_c\rangle \leftrightarrow |0\rangle$ and $|\downarrow_c\rangle \leftrightarrow |1\rangle$ respectively. Due to the narrow linewidth of the 850nm/854nm laser, the Raman transition has a long coherence time of ~ 1 ms (see Fig. S5), so that the optical phases of the beams remain constant over the interval of ~ 10 μ s between two successive Raman pulses. Thus the optical phases are cancelled and the relative phase can be precisely controlled by setting the phases of waveforms in the radio frequency band. We measure the average transfer fidelity by initializing the qubit to six mutually unbiased states (MUB) $|\uparrow\rangle, |\downarrow\rangle, |+\rangle, |-\rangle, |L\rangle, |R\rangle$ encoded on $|\uparrow_c\rangle/|\downarrow_c\rangle$, and applying variable numbers of Raman π -pulses. The average transfer fidelity is measured to be 99.2(2)% per Raman π -pulse for six MUBs (see Fig. 2C).

The network protocol is illustrated in Fig. 3A. After 2.5 ms Doppler cooling and 1.4 ms EIT cooling, we prepare the memory qubit on two basis states $|\uparrow_m\rangle = |D_{5/2}, m = +3/2\rangle$ and $|\downarrow_m\rangle = |D_{5/2}, m = +5/2\rangle$ via optical pumping and 729 nm pulses. The memory qubit is stored for two periods of τ with a spin echo in the middle, and read out at the end. Inside each period of τ , repetitive trials of ion-photon entangling attempts

are performed in a heralded style via an excitation pulse. Once a photon detection event is recorded, the excitation trial halts immediately and state inspection is performed via the Raman conversion, state manipulation, and fluorescence detection. The intermediate cooling is performed every $N = 100$ trials. In each trial, the communication ion is first prepared to the initial state $|S_{1/2}, m = +1/2\rangle$ by 290 ns of optical pumping. A strong picosecond pulse at 397 nm pumps the ion to the excited state $|P_{1/2}, m = -1/2\rangle$ with nearly unity efficiency. The excited state then decays to $|D_{3/2}\rangle$ level with a branching ratio of 6% and emits a photon at 866 nm (see Fig. 1B) [41]. Once this happens, the ion and the photon are prepared into an entangled state, which can be expressed as

$$|\Psi\rangle = \frac{1}{\sqrt{3}}|0\rangle|\pi\rangle + \frac{1}{\sqrt{6}}|1\rangle|\sigma^-\rangle + \frac{1}{\sqrt{2}}|2\rangle|\sigma^+\rangle \quad (1)$$

where $|0\rangle \equiv |D_{3/2}, m = -1/2\rangle$, $|1\rangle \equiv |D_{3/2}, m = +1/2\rangle$, $|2\rangle \equiv |D_{3/2}, m = -3/2\rangle$, and the weights are from the Clebsh-Gordan coefficients of the corresponding transitions. The emitted photon is collected by an objective of NA = 0.52 with the optical axis perpendicular to the magnetic field, and then coupled into a single-mode fiber. In this case, the emission in the $|\pi\rangle$ polarization will be projected to $|H\rangle$, and $|\sigma^\pm\rangle$ will be projected to $|V\rangle$ with a half probability. Thus the entangled state becomes $|\Psi\rangle = \frac{1}{\sqrt{2}}[|0\rangle|H\rangle + (\frac{1}{2}|1\rangle + \frac{\sqrt{3}}{2}|2\rangle)|V\rangle]$. We further combine $\frac{1}{2}|1\rangle + \frac{\sqrt{3}}{2}|2\rangle$ into $|1\rangle$ and convert the ion state to the memory qubit subspace via three successive Raman transitions, including (1) a 850nm/854nm Raman converting $|0\rangle$ to $|\uparrow_c\rangle$, (2) a 866nm/866nm Raman which con-

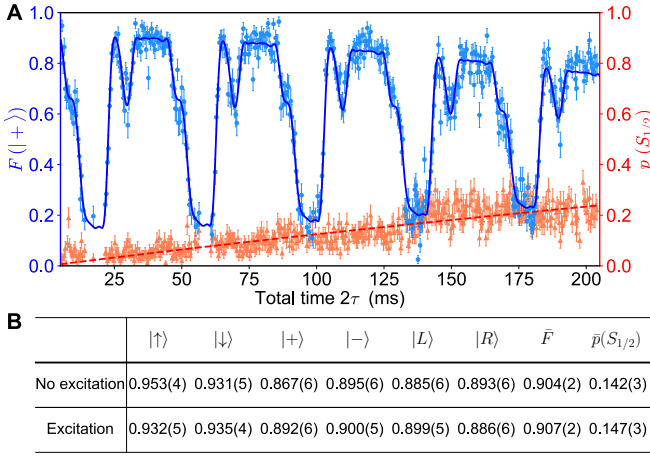


FIG. 4: **Crosstalk-free storage of quantum information in memory qubit.** (A) We measure the decay probability (orange triangle) and the storage fidelity to the initial state $\frac{|\uparrow_m\rangle+|\downarrow_m\rangle}{\sqrt{2}}$ (blue circle) with variable storage time, in the protocol shown in Fig. 3A. (B) The fidelities for six MUBs, average fidelities, and decay probability with/without repetitive cooling, pumping, photon excitation, and state detection on the communication qubit.

verts $\frac{1}{2}(|1\rangle + \frac{\sqrt{3}}{2}|2\rangle)$ to $|1\rangle$, and (3) another 850nm/854nm Raman converting $|1\rangle$ to $|\downarrow_c\rangle$ (see Fig. 2A). After these three Raman transitions, we end up with a maximally entangled Bell state:

$$|\Psi\rangle = \frac{1}{\sqrt{2}}(|\uparrow_c\rangle|H\rangle + |\downarrow_c\rangle|V\rangle) \quad (2)$$

It is noteworthy that the Raman beams will not influence the memory qubit stored in the basis states $|\uparrow_m\rangle$ and $|\downarrow_m\rangle$, as both energy levels will not be driven by 854nm Raman light with the σ^+ polarization. The influence is estimated to be less than 10^{-5} per Raman π -pulse, as shown in Fig. S6. The reason for transferring the communication ion to the memory qubit subspace is that we can use standard 729nm rotations for the qubit state inspection in the next step. If needed, it is not hard to transfer the entangled state back to communication qubit subspace $|\Psi\rangle = \frac{1}{\sqrt{2}}(|0\rangle|H\rangle + |1\rangle|V\rangle)$ via additional 850nm/854nm Raman pulses, or to $|\Psi\rangle = \frac{1}{\sqrt{2}}(|\uparrow_s\rangle|H\rangle + |\downarrow_s\rangle|V\rangle)$ via 729nm pulses ($|\uparrow_s\rangle/|\downarrow_s\rangle \equiv |S_{\frac{1}{2}}, m_s = \mp\frac{1}{2}\rangle$).

The emitted photon at 866 nm can be further converted to 1558 nm on a PPLN (Periodically Poled Lithium Niobate) waveguide surrounded by a Sagnac interferometer in a polarization-maintained style [13, 39]. The external device efficiency about 38% and a signal-to-noise-ratio (SNR) of 22 are achieved by 2.2 W of 1950 nm pumping laser, as shown in Fig. 3D.

We measure the ion-photon entanglement fidelity for three different fiber lengths, i.e. 866 nm photon over a 3 m fiber, 866 nm photon over a 1 km fiber, and converted 1558 nm photon over a 12 km fiber, which represent the network scale of a laboratory, a university campus, and a city, respectively. The inspection of the photonic state is via waveplates and po-

larizers before the photon detector. The inspection for ion states is through 729 nm rotations and a fluorescence detection after the heralding signal of photon detection returns after a round-trip travel time of $2L/c$, where L is the length of fiber and c is the light speed in fiber. Note that the state detection does not influence the memory ion. We use quantum state tomography to characterize the quality of the ion-photon entanglement at 3 m and 1 km. The density matrix of the ion-photon state in these two cases are reconstructed via the MLE (maximum-likelihood estimate) and are illustrated in Fig. 3B and 3C. The measured fidelity to the most close maximally-entangled state is 93.8(3)% over a 3 m fiber with a total storage time $2\tau = 40$ ms. The fidelity decays a little bit to 92.4(4)% at longer storage time $2\tau = 200$ ms, mainly due to increased instability of 729 nm laser power. At a fiber length of 1 km, the fidelity is measured to be 91.2(7)% with a storage time of 200 ms. For the 12 km ion-photon entanglement with 200 ms storage time, we characterize the fidelity by measuring the visibilities for the ion-photon entangled state in three bases σ_x , σ_y and σ_z [42]. By adjusting the phase of the final 729nm $\pi/2$ rotation, we could observe two sinusoidal oscillations in the $|H\rangle + |V\rangle$ and $|H\rangle + i|V\rangle$ bases as shown in Fig. 3E with visibilities of $V_x = 81.9 \pm 10.7\%$ and $V_y = 79.0 \pm 10.4\%$. Thus the entanglement fidelity can be estimated as $F = \frac{1}{4}(1 + V_x + V_y + V_z) = 87.7 \pm 4.5\%$, with $V_z = 89.8 \pm 10.7\%$. The generation rate of heralded ion-photon entanglement over 3 m, 1 km, 12 km fiber is 46 s^{-1} , 3.4 s^{-1} , 0.032 s^{-1} , and the attempting rate is 264 kHz, 49 kHz, 5 kHz, respectively.

In the last step, we verify that the memory ion can protect the stored quantum information from the dissipative operations on the communication qubit. Unlike the ground state, the metastable $|D_{5/2}\rangle$ level has a finite lifetime and will decay to $|S_{1/2}\rangle$ in a timescale of $T_1 \sim 1$ s, which means the stored quantum information will suffer from noticeable degradation if the storage time is comparable to T_1 . The good news is that this error can be probed via fluorescence detection, which means once happened, it can be discarded to avoid influencing the fidelity of the network task, but at a cost of deteriorated efficiency [24, 43–46]. In the protocol of this experiment, after a storage time of 2τ , the memory qubit is analyzed first by a fluorescence detection to probe whether it has decayed to $|S_{1/2}\rangle$ (the first state detection on the memory qubit). If the memory ion is in the bright state, the protocol terminates and starts over. If the memory ion is in the dark state, we rotate the ion state and execute the second state detection to perform single-qubit state tomography on the quantum state.

We characterize the probability of the level decay by the first state detection with variable storage time 2τ , and the fitted lifetime of the memory qubit is found to be $T_1' = 0.79(3)$ s (Fig. 4A). We attribute the deviation from the precise lifetime $T_1 = 1.168(7)$ s of $|D_{5/2}\rangle$ [47] to the leakage from 854 nm and 729 nm beams. We further initialize the memory ion to $|+\rangle = \frac{|\uparrow_m\rangle+|\downarrow_m\rangle}{\sqrt{2}}$ at the beginning of the protocol, and measure the storage fidelity with variable time 2τ , conditioned on that the memory qubit is still in $|D_{5/2}\rangle$ to exclude the influence from T_1' . In this way, the memory dephasing time is found to be $T_2 = 323(19)$ ms, as shown in Fig. 4A. The fi-

delity oscillates with the storage time, and can be well fitted by a double-frequency noise model at 50 Hz and 150 Hz. To confirm that the operations performed on the communication qubit does not influence the memory qubit, we measure the storage fidelities of six mutually unbiased bases (MUBs) with $2\tau = 120$ ms, with or without all the dissipative operations on the communication qubit. We find the average storage fidelity of six bases is $0.907(2)/0.904(2)$ with/without operations on the communication ion, and the averaged decay probability is $0.147(3)/0.142(3)$ with/without operations on the communication ion. Since both of the storage fidelity and decay probability cannot be distinguished considering the statistical error, we confirm the operations on the communication ion does not influence the memory ion.

In summary, we experimentally realize a novel two-ion quantum network node, which can be performed in a

crosstalk-free style and is suitable for distributing quantum entanglement over metropolitan-scale fiber network. Our scheme is useful not only for trapped-ion system, but also suitable for other physical platforms which have long-lived metastable energy levels such as neutral ^{171}Yb atoms in a tweezer array [43–46]. Under current crosstalk-free excitation scheme, we can also switch to ion-photon entanglement at 397nm for higher rate and fidelity on the laboratory scale [14, 15], by only changing the objective in the setup. The remote entangling rate can be substantially increased if high-efficiency quantum wavelength conversion from UV to telecom band is developed [48–50]. It is also important to further improve the remote ion-photon entanglement generation rate. We believe that the enhancements through a cavity [17, 20, 25, 36, 40, 51] or via multiplexing [6, 21, 52–56] are promising approaches towards this goal.

-
- [1] H. J. Kimble, The quantum internet. *Nature* **453**, 1023-1030 (2008).
- [2] S. Wehner, D. Elkouss, R. Hanson, Quantum internet: A vision for the road ahead. *Science* **362** (2018).
- [3] L. Gyongyosi, S. Imre, Advances in the quantum internet. *Commun. ACM* **65**, 52 (2022).
- [4] H. J. Briegel, W. Dür, J. I. Cirac, P. Zoller, Quantum repeaters: The role of imperfect local operations in quantum communication. *Phys. Rev. Lett.* **81**, 5932 (1998).
- [5] L. M. Duan, M. D. Lukin, J. I. Cirac, P. Zoller, Long-distance quantum communication with atomic ensembles and linear optics, *Nature* **414**, 413-418 (2001).
- [6] N. Sangouard, C. Simon, H. D. Riedmatten, N. Gisin, Quantum repeaters based on atomic ensembles and linear optics. *Rev. Mod. Phys.* **83**, 33-80 (2011).
- [7] K. Hammerer, A. S. Sørensen, E. S. Polzik, Quantum interface between light and atomic ensembles. *Rev. Mod. Phys.* **82**, 1041-1093 (2010).
- [8] J. I. Cirac, A. K. Ekert, S. F. Huelga, C. Macchiavello, Distributed quantum computation over noisy channels. *Phys. Rev. A: At., Mol., Opt. Phys.* **59**, 4249-4254 (1999).
- [9] P. Kómár, E. M. Kessler, M. Bishof, L. Jiang, A. S. Sørensen, J. Ye, M. D. Lukin, A quantum network of clocks. *Nat. Phys* **10**, 582-587 (2014).
- [10] D. Gottesman, T. Jennewein, S. Croke, Longer-baseline telescopes using quantum repeaters. *Phys. Rev. Lett.* **109** (2012).
- [11] B. C. Nichol, R. Srinivas, D. P. Nadlinger, P. Drmota, D. Main, G. Araneda, C. J. Ballance, D. M. Lucas, An elementary quantum network of entangled optical atomic clocks. *Nature* **609**, 689-694 (2022).
- [12] D. P. Nadlinger, P. Drmota, B. C. Nichol, G. Araneda, D. Main, R. Srinivas, D. M. Lucas, C. J. Ballance, K. Ivanov, E. Y. Tan, P. Sekatski, R. L. Urbanke, R. Renner, N. Sangouard, J. D. Bancal, Experimental quantum key distribution certified by bell's theorem. *Nature* **607**, 682-686 (2022).
- [13] W. Zhang, T. van Leent, K. Redeker, R. Garthoff, R. Schwonek, F. Fertig, S. Eppelt, W. Rosenfeld, V. Scarani, C. C. Lim, H. Weinfurter, A device-independent quantum key distribution system for distant users. *Nature* **607**, 687-691 (2022).
- [14] L. J. Stephenson, D. P. Nadlinger, B. C. Nichol, S. An, P. Drmota, T. G. Ballance, K. Thirumalai, J. F. Goodwin, D. M. Lucas, C. J. Ballance, High-rate, high-fidelity entanglement of qubits across an elementary quantum network. *Phys. Rev. Lett.* **124**, 110501 (2019).
- [15] J. O'Reilly, G. Toh, I. Goetting, S. Saha, M. Shalaev, A. Carter, A. Risinger, A. Kalakuntla, T. Li, A. Verma, C. Monroe, Fast photon-mediated entanglement of continuously-cooled trapped ions for quantum networking. <https://arxiv.org/abs/2404.16167> (2024).
- [16] P. Drmota, D. Main, D. P. Nadlinger, B. C. Nichol, M. A. Weber, E. M. Ainley, A. Agrawal, R. Srinivas, G. Araneda, C. J. Ballance, D. M. Lucas, Robust quantum memory in a trapped-ion quantum network node. *Phys. Rev. Lett.* **130**, 090803 (2023).
- [17] V. Krutyanskiy, M. Galli, V. Krcmarsky, S. Baier, D. A. Fioretto, Y. Pu, A. Mazloom, P. Sekatski, M. Canteri, M. Teller, J. Schupp, J. Bate, M. Meraner, N. Sangouard, B. P. Lanyon, T. E. Northup, Entanglement of trapped-ion qubits separated by 230 meters. *Phys. Rev. Lett.* **130**, 050803 (2023).
- [18] P. J. Stas, Y. Q. Huan, B. Machielse, E. N. Knall, A. Suleymanzade, B. Pingault, M. Sutula, S. W. Ding, C. M. Knaut, D. R. Assumpcao, Y. C. Wei, M. K. Bhaskar, R. Riedinger, D. D. Sukachev, H. Park, M. Lončar, D. S. Levonian, M. D. Lukin, Robust multi-qubit quantum network node with integrated error detection. *Science* **378**, 557-560 (2022).
- [19] N. Kalb, A. A. Reiserer, P. C. Humphreys, J. J. Bakermans, S. J. Kamberling, N. H. Nickerson, S. C. Benjamin, D. J. Twitchen, M. Markham, R. Hanson, Entanglement distillation between solid-state quantum network nodes. *Science* **356**, 928-932 (2017).
- [20] S. Daiss, S. Langenfeld, S. Welte, E. Distanto, P. Thomas, L. Hartung, O. Morin, G. Rempe, A quantum-logic gate between distant quantum-network modules. *Science* **371**, 614-617 (2021).
- [21] D. Lago-Rivera, S. Grandi, J. V. Rakonjac, A. Seri, H. de Riedmatten, Telecom-heralded entanglement between multimode solid-state quantum memories. *Nature* **594**, 37-40 (2021).
- [22] J.-L. Liu, X.-Y. Luo, Y. Yu, C.-Y. Wang, B. Wang, Y. Hu, J. Li, M.-Y. Zheng, B. Yao, Z. Yan, D. Teng, J.-W. Jiang, X.-B. Liu, X.-P. Xie, J. Zhang, Q.-H. Mao, X. Jiang, Q. Zhang, X.-H. Bao, J.-W. Pan, A multinode quantum network over a metropolitan area. <https://arxiv.org/abs/2309.00221> (2023).
- [23] C. J. Ballance, T. P. Harty, N. M. Linke, M. A. Sepiol, D. M. Lucas, High-fidelity quantum logic gates using trapped-ion hy-

- perfine qubits. *Phys. Rev. Lett.* **117**, 060504 (2016).
- [24] M. P. da Silva, C. Ryan-Anderson, J. M. Bello-Rivas, A. Chernoguzov, J. M. Dreiling, C. Foltz, F. Frachon, J. P. Gaebler, T. M. Gatterman, L. Grans-Samuelssohn, D. Hayes, N. Hewitt, J. Johansen, D. Lucchetti, M. Mills, S. A. Moses, B. Neyenhuis, A. Paz, J. Pino, P. Siegfried, J. Strabley, A. Sundaram, D. Tom, S. J. Wernli, M. Zanner, R. P. Stutz, K. M. Svore, Demonstration of logical qubits and repeated error correction with better-than-physical error rates. <https://arxiv.org/abs/2404.02280> (2024).
- [25] V. Krutyanskiy, M. Canteri, M. Meraner, J. Bate, V. Krucmarsky, J. Schupp, N. Sangouard, B. P. Lanyon, Telecom-wavelength quantum repeater node based on a trapped-ion processor. *Phys. Rev. Lett.* **130**, 213601 (2023).
- [26] M. Bergerhoff, O. Elshehy, S. Kucera, M. Kreis, J. Eschner, Quantum repeater node with free-space coupled trapped ions. <https://arxiv.org/abs/2312.14805v2> (2023).
- [27] Y. F. Pu, S. Zhang, Y. K. Wu, N. Jiang, W. Chang, C. Li, L. M. Duan, Experimental demonstration of memory-enhanced scaling for entanglement connection of quantum repeater segments. *Nat. Photonics* **15**, 374-378 (2021).
- [28] P. Wang, C. Y. Luan, M. Qiao, M. Um, J. Zhang, Y. Wang, X. Yuan, M. Gu, J. Zhang, K. Kim, Single ion qubit with estimated coherence time exceeding one hour. *Nat. Commun.* **12**, 1-8 (2021).
- [29] Monroe, C., Raussendorf, R., Ruthven, A., Brown, K. R., Maunz, P., L. M., Duan, & Kim, J., Large-scale modular quantum-computer architecture with atomic memory and photonic interconnects. *Phys. Rev. A* **89**, 022317 (2014)
- [30] L.-M. Duan, B. B. Blinov, D. L. Moehring, C. Monroe, Scalable trapped ion quantum computation with a probabilistic ion-photon mapping. *Quantum Information and Computation* **3**, 165 (2004).
- [31] L.-M. Duan, C. Monroe, Colloquium: Quantum networks with trapped ions. *Rev. Mod. Phys.* **82**, 1209 (2010)
- [32] H. X. Yang, J. Y. Ma, Y. K. Wu, Y. Wang, M. M. Cao, W. X. Guo, Y. Y. Huang, L. Feng, Z. C. Zhou, L. M. Duan, Realizing coherently convertible dual-type qubits with the same ion species. *Nat. Phys.* **18**, 1058-1061 (2022).
- [33] L. Feng, Y. Y. Huang, Y. K. Wu, W. X. Guo, J. Y. Ma, H. X. Yang, L. Zhang, Y. Wang, C. X. Huang, C. Zhang, L. Yao, B. X. Qi, Y. F. Pu, Z. C. Zhou, L. M. Duan, Realization of a crosstalk-avoided quantum network node using dual-type qubits of the same ion species. *Nat. Commun.* **15**, 1-7 (2024).
- [34] D. T. Allcock, W. C. Campbell, J. Chiaverini, I. L. Chuang, E. R. Hudson, I. D. Moore, A. Ransford, C. Roman, J. M. Sage, D. J. Wineland, omg blueprint for trapped ion quantum computing with metastable states. *Appl. Phys. Lett.* **119**, 214002 (2021).
- [35] B. Casabone, C. Deshmukh, S. Liu, D. Serrano, A. Ferrier, T. Hümmer, P. Goldner, D. Hunger, H. de Riedmatten, Dynamic control of Purcell enhanced emission of erbium ions in nanoparticles. *Nat. Commun.* **12**, 1-7 (2021).
- [36] A. M. Dibos, M. Raha, C.M. Phenicie, J. D. Thompson, Atomic Source of Single Photons in the Telecom Band. *Phys. Rev. Lett.* **120**, 243601 (2018).
- [37] A. G. Radnaev, Y. O. Dudin, R. Zhao, H. H. Jen, S. D. Jenkins, A. Kuzmich, T. A. Kennedy, A quantum memory with telecom-wavelength conversion. *Nat. Phys.* **6**, 894-899 (2010).
- [38] W. Chang, C. Li, Y. K. Wu, N. Jiang, S. Zhang, Y. F. Pu, X. Y. Chang, L. M. Duan, Long-distance entanglement between a multiplexed quantum memory and a telecom photon. *Phys. Rev. X* **9**, 041033 (2019).
- [39] R. Ikuta, T. Kobayashi, T. Kawakami, S. Miki, M. Yabuno, T. Yamashita, H. Terai, M. Koashi, T. Mukai, T. Yamamoto, N. Imoto, Polarization insensitive frequency conversion for an atom-photon entanglement distribution via a telecom network. *Nat. Commun.* **9**, 1-8 (2018).
- [40] T. Walker, K. Miyanishi, R. Ikuta, H. Takahashi, S. V. Koshaniyan, Y. Tsujimoto, K. Hayasaka, T. Yamamoto, N. Imoto, M. Keller, Long-distance single photon transmission from a trapped ion via quantum frequency conversion. *Phys. Rev. Lett.* **120**, 203601 (2018).
- [41] M. Ramm, T. Pruttivarasin, M. Kokish, I. Talukdar, H. Häffner, Precision measurement method for branching fractions of excited $P_{1/2}$ states applied to $^{40}\text{Ca}^+$. *Phys. Rev. Lett.* **111**, 023004 (2013).
- [42] Y. Yu, F. Ma, X.-Y. Luo, B. Jing, P.-F. Sun, R.-Z. Fang, C.-W. Yang, H. Liu, M.-Y. Zheng, X.-P. Xie, W.-J. Zhang, L.-X. You, Z. Wang, T.-Y. Chen, Q. Zhang, X.-H. Bao, J.-W. Pan, Entanglement of two quantum memories via fibers over dozens of kilometres. *Nature* **578**, 240 (2020).
- [43] J. W. Lis, A. Senoo, W. F. McGrew, F. Rönchen, A. Jenkins, A. M. Kaufman, Midcircuit operations using the omg architecture in neutral atom arrays. *Phys. Rev. X* **13**, 041035 (2023).
- [44] M. A. Norcia, W. B. Cairncross, K. Barnes, P. Battaglini, A. Brown, M. O. Brown, K. Cassella, C. A. Chen, R. Coxe, D. Crow, J. Epstein, C. Griger, A. M. Jones, H. Kim, J. M. Kindem, J. King, S. S. Kondov, K. Kotru, J. Lauigan, M. Li, M. Lu, E. Megidish, J. Marjanovic, M. McDonald, T. Mitiga, J. A. Muniz, S. Narayanaswami, C. Nishiguchi, R. Notermans, T. Paule, K. A. Pawlak, L. S. Peng, A. Ryou, A. Smull, D. Stack, M. Stone, A. Sucich, M. Urbanek, R. J. V. D. Veerdonk, Z. Vendeiro, T. Wilkason, T. Y. Wu, X. Xie, X. Zhang, B. J. Bloom, Midcircuit qubit measurement and rearrangement in a ^{171}Yb atomic array. *Phys. Rev. X* **13**, 041034 (2023).
- [45] W. Huie, L. Li, N. Chen, X. Hu, Z. Jia, W. K. C. Sun, J. P. Covey, Repetitive readout and real-time control of nuclear spin qubits in ^{171}Yb atoms. *PRX Quantum* **4**, 030337 (2023).
- [46] S. Ma, G. Liu, P. Peng, B. C. Zhang, S. Jandura, J. Claes, A. P. Burgers, G. Pupillo, S. Puri, J. D. Thompson, High-fidelity gates and mid-circuit erasure conversion in an atomic qubit. *Nature* **622**, 279 (2023).
- [47] P. A. Barton, C. J. Donald, D. M. Lucas, D. A. Stevens, A. M. Steane, D. N. Stacey, Precision measurement of the lifetime of the $3d^2D_{5/2}$ state in $^{40}\text{Ca}^+$. *Phys. Rev. A* **62**, 032503 (2000).
- [48] H. Rütz, K.-H. Luo, H. Suche, C. Silberhorn, Quantum frequency conversion between infrared and ultraviolet. *Phys. Rev. Appl.* **7**, 024021 (2017).
- [49] S. Kasture, F. Lenzi, B. Haylock, A. Boes, A. Mitchell, E. W. Streed, M. Lobino, Frequency conversion between uv and telecom wavelengths in a lithium niobate waveguide for quantum communication with Yb^+ trapped ions. *Journal of Optics* **18**, 104007 (2016).
- [50] J. Hannegan, U. Saha, J. D. Siverns, J. Cassell, E. Waks, Q. Quraishi, C-band single photons from a trapped ion via two-stage frequency conversion. *Appl. Phys. Lett.* **119**, 84001 (2021).
- [51] K. Tanji, H. Takahashi, W. Roga, M. Takeoka, Rate-fidelity trade-off in cavity-based remote entanglement generation. <https://arxiv.org/abs/2403.15179> (2024).
- [52] Y. F. Pu, N. Jiang, W. Chang, H. X. Yang, C. Li, L. M. Duan, Experimental realization of a multiplexed quantum memory with 225 individually accessible memory cells. *Nat. Commun.* **8**, 15359 (2017).
- [53] S. Zhang, J. X. Shi, Z. B. Cui, Y. Wang, Y. K. Wu, L. M. Duan, Y. F. Pu, Realization of a programmable multi-purpose photonic quantum memory with over-thousand qubit manipula-

- tions. *Phys. Rev. X* **14**, 021018 (2023).
- [54] S. Zhang, X. J. Shi, Y. B. Liang, Y. D. Sun, Y. K. Wu, L. M. Duan, Y. F. Pu, Fast delivery of heralded atom-photon quantum correlation over 12km fiber through multiplexing enhancement. <https://arxiv.org/abs/2403.13623> (2024)
- [55] V. Krutyanskiy, M. Canteri, M. Meraner, V. Krcmarsky, B. P. Lanyon, Multimode Ion-Photon Entanglement over 101 Kilometers. *PRX Quantum* **5**, 020308 (2024).
- [56] B. You, Q. Wu, D. Miron, W. Ke, I. Monga, E. Saglamyurek, H. Haeffner, Temporally multiplexed ion-photon quantum interface via fast ion-chain transport. <https://arxiv.org/abs/2405.10501> (2024)
- [57] A. Stute, "A light-matter quantum interface: ion-photon entanglement and state mapping," thesis, University of Innsbruck, Innsbruck, Tirol. Austria (2012).

Acknowledgements: We acknowledge helpful discussions with Lai Zhou, Chi Zhang, Lu Feng, Panyu Hou, and Ye Wang.

Funding: This work is supported by Innovation Program for Quantum Science and Technology (No.2021ZD0301604), the

Tsinghua University Initiative Scientific Research Program and the Ministry of Education of China through its fund to the IIIS. Y.F.P. acknowledges support from the start-up fund and the Dushi Program from Tsinghua University. Y.K.W. acknowledges support from the start-up fund from Tsinghua University.

Author Contributions: P.C.L., Y. W., J.X.S. Z.B.C., Z.Q.W., S.Z., P.Y.L., Z.C.T., Y.D.S., X.Y.C., B.X.Q., Y.Y.H., Z.C.Z. and Y.F.P. carried out the experiment. Y.F.P. and L.M.D. supervised the project. All the authors contributed to the discussion and the writing.

Competing interests: X.Y.C., B.X.Q., Y.Y.H., Z.C.Z., Y.K.W., Y.X., Y.F.P. and L.M.D. hold shares with HYQ Co. The other authors declare no competing interests.

Data and materials availability: All data needed to evaluate the conclusions in the paper are present in the paper and/or the Supplementary Materials.

Supplementary Materials for Realization of a crosstalk-free multi-ion node for long-distance quantum networking

I. LEVEL STRUCTURE AND LASER BEAM DIAGRAM

Fig. S1 shows the level structure of $^{40}\text{Ca}^+$. In our experiment, ion is initialized in $|S_{1/2}, m = +1/2\rangle$ by optical pumping with σ^+ -polarized 397 nm continuous laser beam and 866 nm beam. Doppler cooling, electromagnetically induced transparency (EIT) cooling and fluorescence detection are also performed by 397 nm laser beam and 866 nm beam. Fig. S2 shows the diagram of laser beams. The addressed 729 nm beam is perpendicular to the plane and not shown.

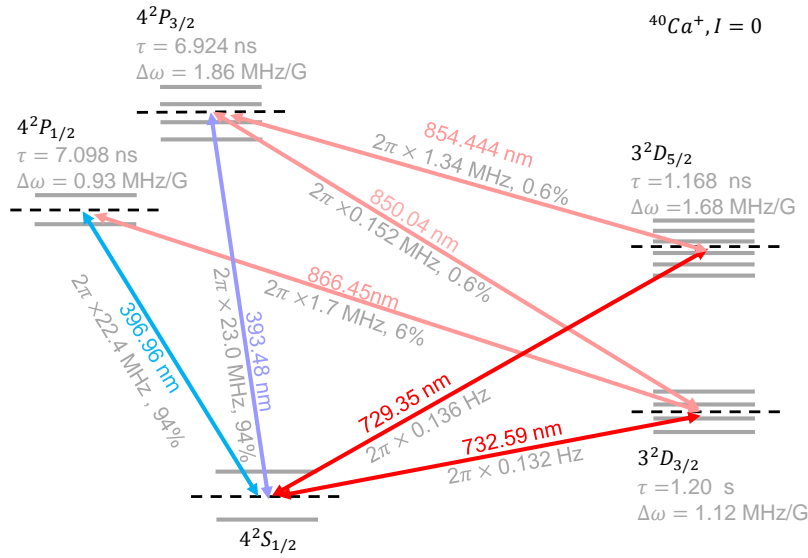


FIG. S1: $^{40}\text{Ca}^+$ ion energy level structure [57]. We list all the energy levels and transitions of $^{40}\text{Ca}^+$ ion in this figure.

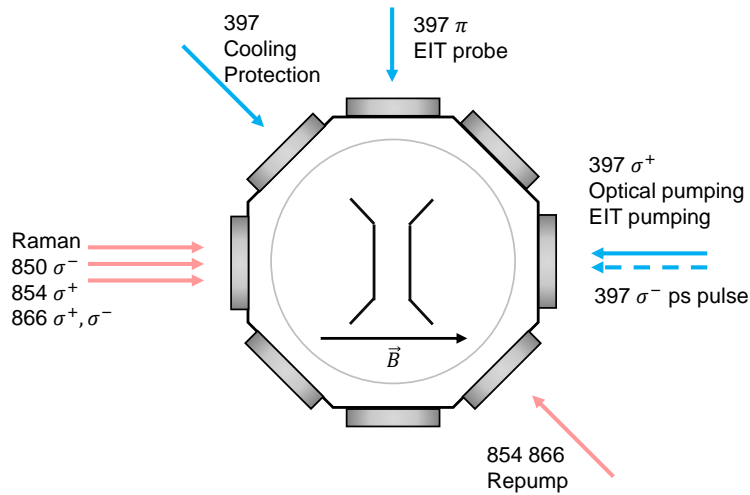


FIG. S2: **Laser beam diagram.** The laser scheme in our experiment.

II. CONTROL SYSTEM

For specific purpose of heralded entanglement experiments, a home-made device “QNetWorker” handling the entanglement attempts with high speed and precision of decision making process has to be developed, in cooperation with the other programmable logic unit “Sequencer”, which controls usual sequences and offers the flexibility of managing the overall branch of decision for all qubits to enable swift scheduling of entanglements generation and subsequent operation.

The QNetWorker functions in entanglement establishment alongside encoding transfer for network qubits with logic controls as the following content encapsulates:

- TTL outputs for controlling 397 nm and 866 nm laser beam’s RF switches, for driving corresponding AOM for state preparation and providing the pulse picker with EOM trigger, which composes the trial sequence up to 1 MHz repetition rate, mainly limited by AOM latency.
- Four input channels with separately adjustable time window for acquiring signal of SNSPD. Facilitating timestamps readout of heralded events with superior precision of 417 ps (2 ns adopted in this work).
- Decisions of consecutive sequences to manipulate communication qubits based on heralding patterns encoded in a 4-bit word of input events without latency. Moreover, the subsequent sequences are synchronized with the timestamps, for minimized 866nm Raman transition phase error for merging gate.
- Redundant interfaces of modules facilitates the potential to programmable modulations by adequate digital output channels such as feedforward phase correction of 866nm Raman merging gate (not in this work) and controlling sequences of arbitrary waveform generator based on heralding patterns and experiment design.

Furthermore, Sequencer serves as the master controller of experiment sequences which regulates QNetWorker for entangling trials. It enables immediate detection right after heralding events or in-sequence manipulations and detection of communication qubits during arbitrary gate sequences such as spin echo of memory qubits. In principle, any sophisticated gates implementation could be accomplished in current system.

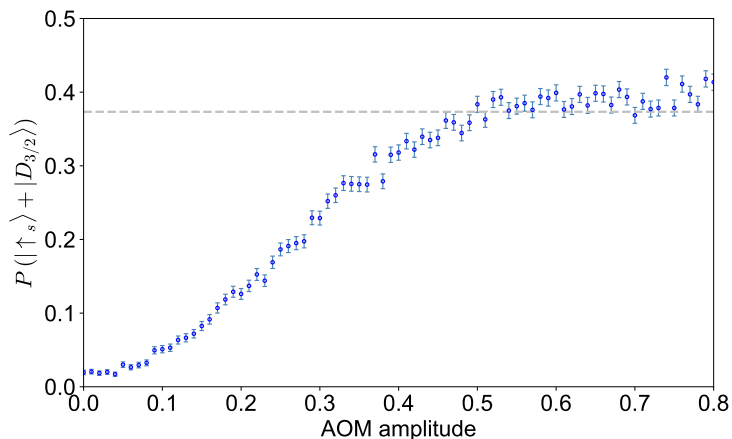


FIG. S3: **Calibration of pulse laser.** We verify a single 397 nm pulse can drive a π -pulse by measuring the proportion of state pumped to $|\uparrow_s\rangle \equiv |S_{1/2}, m = -1/2\rangle$ and $|D_{3/2}\rangle$ after excitation, with variable pulse energy.

III. PULSE EXCITATION

In the experiment, we use 397 nm pulse laser with σ^- polarization to excite ion from $|S_{1/2}, m = +1/2\rangle$ to $|P_{1/2}, m = -1/2\rangle$. After pulse excitation and spontaneous decay of ion, population in $|S_{1/2}, m = -1/2\rangle$ and $|D_{3/2}\rangle$ is measured. The outcome of the calibration process is shown in Fig. S3, with which we get the corresponding AOM amplitude to achieve pulse area of π . The dashed line shows the theoretical population in $|S_{1/2}, m = -1/2\rangle$ and $|D_{3/2}\rangle$ for π -pulse. State preparation and shelving error account for the fraction exceeding theoretical value. After determination of π -pulse AOM amplitude, we verify that the 397 nm pulse laser will not off-resonantly drive the ion to $|P_{3/2}\rangle$, and induce the ion to fall out of the 3-level communication subspace,

which results in $|3D_{5/2}\rangle$ population. We excite ion from $|S_{1/2}, m = +1/2\rangle$ to $|P_{1/2}, m = -1/2\rangle$ repeatedly and measure the state of ion. Pulse excitations for over 10^6 times gives no $3D_{5/2}$ population, which verifies pulse laser in our experiment will not give rise to excitation from $|4S_{1/2}\rangle$ to $|4P_{3/2}\rangle$.

We plot the histogram for the arrival time of 866 nm photon relative to pulse excitation trigger. Fig. S4 shows the time distribution of photon collected. Latency, jitters and exponential decay of ion give rise to the shape of the histogram. We fit the histogram with convolution of Gaussian distribution and exponential decay, and the fitted $1/e$ decay time is 6.936 ± 0.147 ns. In the experiment, we record timestamps of photon detected by single photon detector and optimize the detection window accordingly to achieve a high signal to noise ratio.

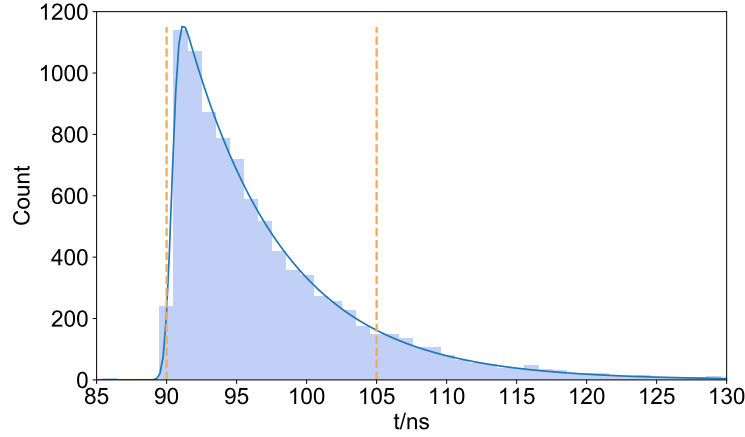


FIG. S4: **Photon distribution.** The histogram of photon arrival time relative to the excitation trigger. The 15-ns acceptance window of photons is between the two dashed lines.

IV. 850 & 854 RAMAN

Fig. S5A shows 850 nm and 854 nm laser locking scheme. They are locked to the same reference cavity in the experiment. 850 & 854 Raman Ramsey fringe between $|D_{3/2}, m = -1/2\rangle$ and $|D_{5/2}, m = -5/2\rangle$ is measured, fitting to a Gaussian decay gives a Raman coherence time of $1019 \pm 34 \mu\text{s}$.

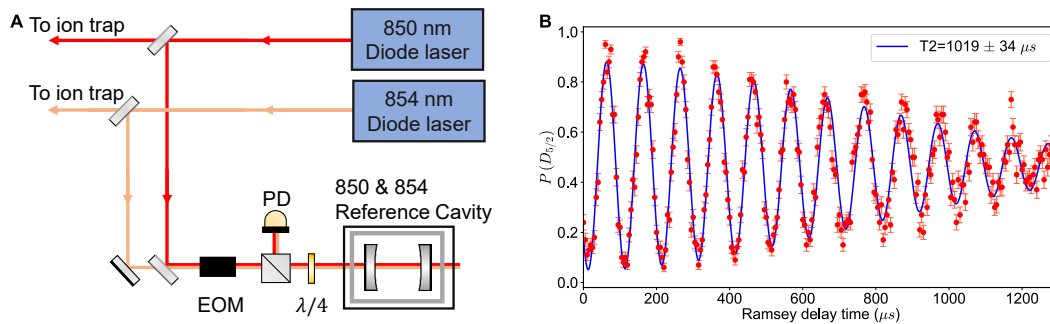


FIG. S5: **850 nm & 854 nm laser locking scheme and Raman Ramsey.** (A) Locking schemes for two lasers. (B) Raman Ramsey fringe measurement.

In the experiment, 850 & 854 Raman transitions transfer qubits between two subspaces. The Raman pulse should not influence the memory qubit due to polarization and frequency mismatch. We prepare memory qubit to $|+\rangle = \frac{|\uparrow_m\rangle + |\downarrow_m\rangle}{\sqrt{2}}$ and measure population of $|S_{1/2}\rangle$ to detect the unwanted scattering, with 850 & 854 Raman laser on or off. As shown in Fig. S6, we cannot observe any notable difference between two cases in a duration of approximately 1000 π -pulses. The population decay happens with a chance $< 10^{-5}$ for each π -pulse.

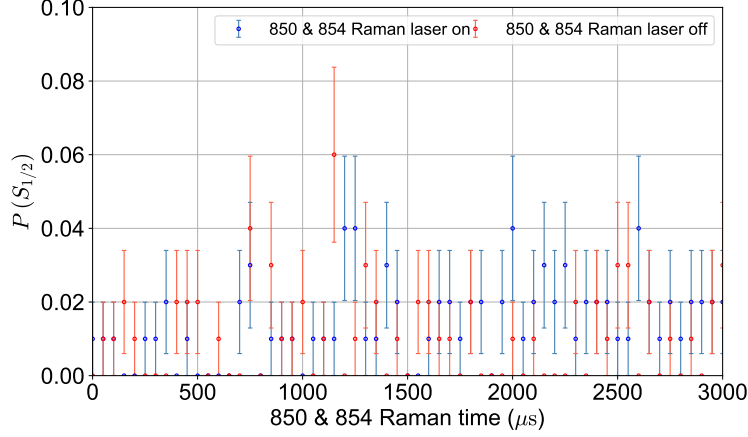


FIG. S6: **Influence of 850 & 854 Raman transition to memory qubit population.** We measure the unwanted scattering probability of Raman transitions with variable Raman interaction time.

V. POLARIZATION PRESERVING QFC AND SPECTRUM FILTERING

Our frequency conversion device to telecom C-band is realized via difference frequency generation (DFG) process in a periodically poled lithium niobate (PPLN) waveguide. The 1.5 cm waveguide is placed at the center of a Sagnac type interferometer to achieve polarization preserving. Temperature of the waveguide is set to 71.5°C to meet the best quasi-phase-matching condition.

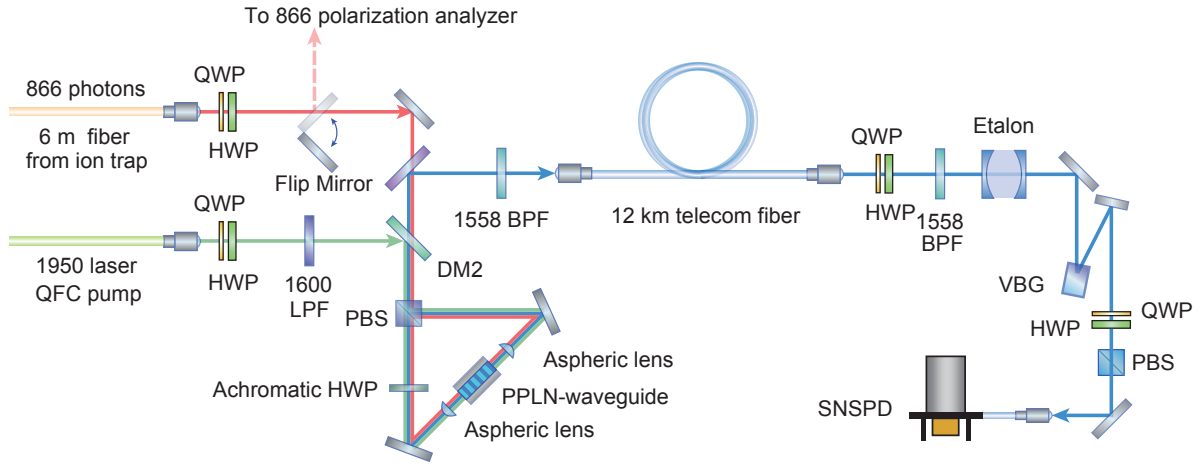


FIG. S7: **The PPQFC and spectrum filtering setup.** The setup diagram for the quantum frequency conversion module.

As illustrated in Fig. S7, the 866 nm signal photons are mixed with a strong 1950 nm CW pump field by a dichroic mirror and then sent into the Sagnac interferometer. Here the beam is divided into two arms in accordance with its polarization on the PBS (customized for three wavelengths). One arm with H polarizing is then flip to V polarizing on an achromatic half wave plate to meet the phase matching polarization of the PPLN-waveguide. We place two aspheric lenses symmetrically to couple 866 nm photons and 1950 nm pump field together into PPLN-waveguide on dual ends with about 80% coupling efficiency. Both the aspheric lenses and our waveguide have customized anti-reflective coatings for all three wavelengths. After the 866 nm signal photons are converted to 1558 nm in the waveguide, they travel along the rest parts of the interferometer and coherently combined to 1558 nm polarization qubits on the PBS. Finally converted photons are picked out by a dichroic mirror and collected into a 12 km G652D telecom-fiber with 80% coupling efficiency.

To suppress the background noise and reach a high signal-background ratio, several types of spectrum filters are utilized, as shown in Fig. S8. The 1950 nm pump laser is filtered by a long pass filter to eliminate its amplified spontaneous emission (ASE) at 1558 nm. In our wavelength selection, the prominent background noise in the QFC process comes from anti-Stokes Raman

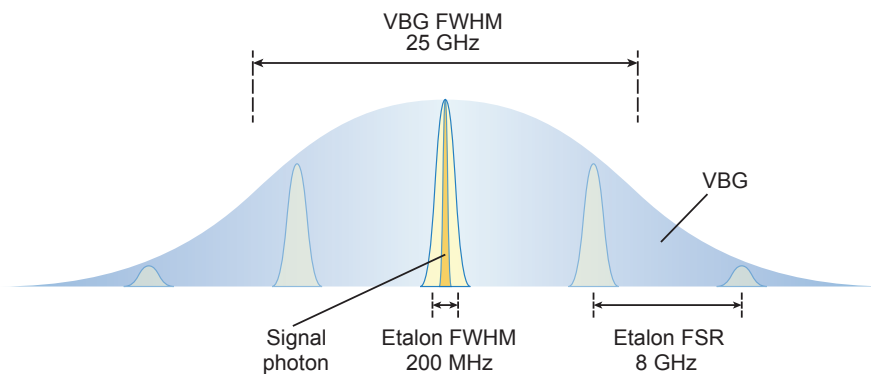


FIG. S8: **Narrow spectrum transmission window.** The transmission spectrum for different filters and the photon linewidth.

scattering of strong 1950 nm pump field. The measured Raman scattering background at 1558 nm is about 5 kHz/nm with 1.1 W 1950 nm pumping, which makes a narrow-band spectral filtering system for converted photons necessary. Here in our setup, two band pass filters (FWHM 5 nm, Center 1558 nm) first remove the major part of the residual 1950 nm pump laser and other stray light from 1558 nm converted photons. Then the photons subsequently pass a highly stable filtering etalon (FSR 8 GHz, FWHM 200 MHz, 90% transmission) and a volume Bragg grating (VBG, FWHM 25 GHz, 98% reflection efficiency). This combination determines a 200 MHz narrow spectrum transmission window which suppresses the Raman background to 8 Hz under 1.1 W 1950 nm CW pumping. Taking the dark count rate of SNSPD into consideration, the total background noise is 18 Hz and the signal background ratio is up to 22.